Plasma tomographic reconstruction from tangentially viewing camera with background subtraction — Source link ↗

Michal Odstrcil, J. Mlynář, Vladimir Weinzettl, P. Hacek ...+5 more authors

Institutions: Max Planck Society, Ghent University, Hungarian Academy of Sciences

Topics: Tomographic reconstruction, Background subtraction, Tomography, Specular reflection and Iterative reconstruction

Related papers:

- 3D reconstruction of specular surfaces using a calibrated projector–camera setup

- 3D reconstruction of specular surface via a novel structured light approach

- Specular Reflection Separation Using Dark Channel Prior

- Calibrating light sources by using a planar mirror

- 1 0-5 3D Reconstruction of Skin Surface from Image Sequence

Share this paper: 📘 🐦 in ✉

View more about this paper here: https://typeset.io/papers/plasma-tomographic-reconstruction-from-tangentially-viewing-1vx9u623z4

Plasma tomographic reconstruction from tangentially viewing camera with background subtraction

M. Odstril, J. Mlyná, V. Weinzettl, P. Háek, T. Odstril, G. Verdoolaege, M. Berta, T. Szabolics, and A. Bencze

CrossMark
click for updates

Plasma tomographic reconstruction from tangentially viewing camera with background subtraction

M. Odstrčil,[1,a)] J. Mlynář,[2] V. Weinzettl,[2] P. Háček,[2] T. Odstrčil,[3] G. Verdoolaege,[4]
M. Berta,[2,5] T. Szabolics,[6] and A. Bencze[6]

[1]*Optical Research Center, University Southampton, Southampton, United Kingdom*
[2]*Institute of Plasma Physics ASCR, Association EUROATOM/PPP.CR Prague, Czech Republic*
[3]*Max-Planck-Institut für Plasmaphysik, Garching, Germany*
[4]*Department of Applied Physics, Ghent University, B-9000 Ghent, Belgium and Association EURATOM –*
Belgian State, Laboratory for Plasma Physics, Koninklijke Militaire School Ecole Royale Militaire,
B-1000 Brussels, Belgium
[5]*Szechenyi Istvan University, Association EUROATOM/HAS, Gyor, Hungary*
[6]*Institute for Particle and Nuclear Physics, Wigner Research Centre for Physics, Hungarian Academy of*
Sciences, Association EUROATOM/HAS, Budapest, Hungary

Light reflections are one of the main and often underestimated issues of plasma emissivity reconstruction in visible light spectral range. Metallic and other specular components of tokamak generate systematic errors in the optical measurements that could lead to wrong interpretation of data. Our analysis is performed at data from the tokamak COMPASS. It is a D-shaped tokamak with specular metallic vessel and possibility of the H-mode plasma. Data from fast visible light camera were used for tomographic reconstruction with background reflections subtraction to study plasma boundary. In this article, we show that despite highly specular tokamak wall, it is possible to obtain a realistic reconstruction. The developed algorithm shows robust results despite of systematic errors in the optical measurements and calibration. The motivation is to obtain an independent estimate of the plasma boundary shape. © 2014 AIP Publishing LLC. [http://dx.doi.org/10.1063/1.4862652]

I. INTRODUCTION

In recent years, fast visible light cameras have become standard equipment of many tokamaks. Usually, cameras are used for observation of plasma-wall interaction, however there are many other applications, e.g., plasma shape, fluctuation, or dust studies.[1–5]

The plasma edge emits visible radiation mainly because of interaction of neutral particles flux from wall with plasma. Projections along lines of sight (LoS) of this emissivity are afterwards detected. Radiation from cool plasma edge can be used to estimate position of radiative shells.

The cameras are usually installed in tokamaks so that the plasma is observed either in poloidal plane (perpendicular view) or toroidal direction (tangential view). The poloidal view is mostly used for bolometry and soft X-ray pin-hole cameras. It is less suitable for line radiation in the visible spectra because the radiative shell placed near to the plasma edge results in flat projections of the hollow emissivity profile. On the other hand, the tangential configuration is often used to observe the plasma edge and divertor regions.[2–4,6] The lines of sights tangential to the plasma column lead to higher contrast in the projections. Moreover, numerical tests proved that the local plasma emissivity can be reconstructed from one 2D image camera, hence one camera is sufficient for a reconstruction, even though the coverage in the projection space[7] is rather narrow. Using the assumption of toroidal symmetry and field of view covering sufficient part of the plasma, the local emissivity can be inferred using tomographic methods.

The tangential camera geometry setup is more challenging compared to the poloidal and pinhole setups because different effects of the used optical system, e.g., image distortion or camera vibration, need to be deducted. Furthermore, fast plasma fluctuations cannot be any longer considered as toroidally symmetrical and the helical geometry should be accounted for. The toroidal symmetry is valid only if the integration time is long enough to smooth out all rapidly moving helical structures. However, inclusion of the safety factor will "hardwire" the expected plasma shape and position into the reconstruction geometry matrix Eq. (1). This represents an *a priori* knowledge which, if false, may damage the result, therefore infinite safety factor was used in this work.

Basically, two kinds of information about plasma can be reconstructed: plasma boundary position, shape,[1,8,9] and fast fluctuations[2,5,6] – i.e., filaments and blobs. The filaments are expected to be significantly elongated along magnetic field, otherwise the conditions for the tomographic reconstruction would not be fulfilled. Finally, reflections from the vessel components can disturb the reconstruction.[9–13] Particularly, in the case of the plasma shape reconstruction, reflections from the vessel wall and in-vessel components are of major importance unlike the case of fast fluctuations where the slowly evolving background can be subtracted. In particular, our data obtained from the tokamak COMPASS[14] with a specular steel vessel wall are significantly affected by light reflections.

II. TANGENTIAL TOMOGRAPHY

Plasma tomography is generally an ill-posed task that transforms line integrated emissivity (i.e., plasma projections)

---

a)mo1e13@soton.ac.uk

to local radiant flux density (typically to plasma cross-sections). Poloidal plasma tomography is a relatively well investigated problem and the corresponding methods are well established and widely used.[7,15] At the same time, the tangential tomography is based on rather basic methods; e.g., truncated singular value decomposition (SVD) or linear methods have been used.[2,5,6,8,9] One of the reasons are the higher computational demands of the tangential tomography.

The main distinction between the tangential camera tomography compared to the poloidal 1D field of detectors is an enormous number of lines of sight while the information is strongly correlated. As a result, although tomographic task can be mathematically overdetermined system, it is still an ill-posed task with lack of information for a direct inversion. Therefore, before the reconstruction, it is recommended to either down-sample data to an optimal size or decompose into low-dimensional orthogonal base vectors, e.g., Bessel or Cormack base in order to increase solving speed and limit the correlations.

Finally, reflections from the tokamak vessel and plasma facing components (PFC) must be subtracted. This is very important because the reflections along with imprecise geometry setting cause systematic errors which can limit reliability of the resulting reconstruction (see Sec. V).

A. Pixel based tomography method with nonlinear constrains

In the pixel-based tomography methods, the unknown two-dimensional (2D) emissivity cross-section $g(x, y)$ is discretized to N_g values g_j in a finite number of pixels $j \in 1, \ldots, N_g$. The unknown reconstruction **g** is searched so that it minimizes residuals with the measured projections **f**, i.e., the line-integrated data and reconstructed emissivity projections.

After discretization of the emissivity to the pixel grid, the task corresponds to a set of linear equations:

$$f_i = \sum_{j=1}^{N} \mathbb{T}_{ij} g_j + \xi_i \quad i \in 1, \ldots, L, \tag{1}$$

where $\mathbb{T}_{ij}$ denotes the geometric (contribution) matrix, g_j is the emissivity in the jth pixel, $\xi_i \sim \mathcal{N}(0, \sigma_i^2)$ represents statistical noise assuming a normal distribution of the projections f_i, and L is the number of measurements. The read-out and discretization noise intensity can be estimated from dark frames, however it is usually negligible. The main sources of error are reflected light and imperfections in the geometry calibration.

This system of equations is ill-posed and, in the case of fusion diagnostic systems, usually underdetermined.

One of the most common methods that finds a trustworthy solution is the Tikhonov regularization which minimizes the reconstruction residual constrained to a regularization function $O(\mathbf{g})$:

$$\min_g \left(\|\mathbb{T}\mathbf{g} - \mathbf{f}\|_2^2 + \lambda O(\mathbf{g}) \right), \tag{2}$$

where $\|\mathbb{T}\mathbf{g} - \mathbf{f}\|_2^2$ is quadratic misfit (the residual) and λ is the regularization parameter. The object function $O(\mathbf{g})$ imposes some realistic *a priori* information, e.g., expected emissivity smoothness, entropy, or probability distribution.

In this contribution, a non-linear regularization function $O(\mathbf{g})$ similar to the minimum Fisher information method[16,17] was implemented:[18]

$$O(\mathbf{g}) = \int \sum_{i,j=1}^{2} \left(\left| \frac{\partial \mathbf{g}}{\partial x_i} \frac{\partial \mathbf{g}}{\partial x_j} \right| + \beta \right) \cdot \begin{cases} \dfrac{1}{\mathbf{g}^\alpha} \, dxdy & g_i > \epsilon \\[2mm] \dfrac{1}{\epsilon} \, dxdy & g_i \le \epsilon \end{cases}, \tag{3}$$

where ϵ is a small positive number. The proposed $O(\mathbf{g})$ regularizes Eq. (2) by enforcing sufficient and physically relevant smoothness and positivity to the reconstructed image. Moreover, the α, β terms suppress large flat non-zero artifacts caused by the background reflection (see Sec. III).

The Tikhonov regularization Eq. (2) with a regularization matrix $\mathbb{H}$ leads to a sparse system that is solved by the Cholesky decomposition:

$$\mathbb{A}\mathbf{g} = (\mathbb{T}^T \mathbb{T} + \lambda \mathbb{H})\mathbf{g} = \mathbb{T}^T \mathbf{f}. \tag{4}$$

The regularization parameter λ sets the strength of an *a priori* constraint $O(\mathbf{g})$ with respect to the value of the residual $\|\mathbb{T}\mathbf{g} - \mathbf{f}\|_2^2$. Underestimated value of λ results in over-fitting and the other extreme leads to over-smoothing. The optimal value of λ was chosen to minimize the χ^2 score of the Pearson distribution:

$$\chi^2 = \sum_{i=1}^{L} \frac{\left(\sum_{j=1}^{N_g} \mathbb{T}_{ij} g_j - f_i \right)^2}{\sigma_i^2}, \tag{5}$$

where L denotes degrees of freedom. Two examples of the χ^2 dependence on the smoothness penalty are displayed in Fig. 8.

The proposed regularization term $O(\mathbf{g})$ Eq. (3) is nonlinear, however it can be solved iteratively using the regularization matrix $\mathbb{H}$,[16] which introduces a discretized and linearized regularization term $O(\mathbf{g})$. $\mathbb{H}$ is implemented in the form:

$$\mathbb{H}^{(k)} = \sum_{l} \mathbb{B}_l^T \mathbb{W}^{(k)} \mathbb{B}_l + \beta \mathbb{W}^{(k)}. \tag{6}$$

$W^{(k)}$ denotes kth iteration of the weighting matrix $\mathbb{W}_{ij}^{(k)} = \delta_{ij} / \mathbf{g}_j^{\alpha,(k-1)}$ and B_i denotes matrices of the discrete derivatives, corresponding to the difference operator. The constants α and β should be optimized over many frames to obtain a smooth and artifact suppressed reconstruction.

Consequently, the tomography algorithm consists of two nested cycles. The inner cycle interpolates λ and minimizes the residuals, while the outer cycle optimizes the weighting matrix $\mathbb{W}$.

III. REFLECTIONS MODEL

Background reflections are one of the important, however often neglected, sources of systematic errors in the case of visible light emissivity measurements. Reflectivity can be described by the bidirectional reflectance distribution function (BRDF) that is defined as the ratio between the incoming irradiance and the outgoing radiance.[19] Two widely
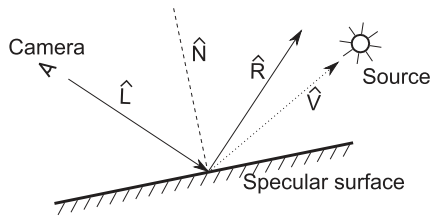
FIG. 1. An illustration of the direction of the vectors used in the reflective models.

used models are the Lambertian and Phong models. The Lambertian model expects a BRDF that is constant and independent of the incidence angle, i.e., matte surface,

$$f_{r,\text{Lambert}} = c_l,$$

where c_l is a material constant. The Phong model is used for specular surfaces and it depends on the angle between the ideally reflected ray **R** and the incident light vector **L** (see Fig. 1),

$$f_{r,\text{Phong}}(\mathbf{L}, \mathbf{R}) = c_p \cos^{c_s} \alpha \,,$$

where c_p, c_s denotes another material constants. Constants c_l, c_p corresponds to the reflectivity of the surface, while c_s is related to its specularity. Large c_s results in mirror-like reflection, while $c_s = 0$ is the Lambertian model. The reflection vector **R** corresponds to

$$\mathbf{R} = 2(\hat{\mathbf{N}} \cdot \mathbf{L})\hat{\mathbf{N}} - \mathbf{L} \,,$$

where $\hat{\mathbf{N}}$ denotes a unit vector normal to the surface (the hat denotes vectors normalized to unity). The reflectance angle is equal to

$$(\hat{\mathbf{R}} \cdot \hat{\mathbf{V}}) = 2(\hat{\mathbf{N}} \cdot \hat{\mathbf{L}})(\hat{\mathbf{N}} \cdot \hat{\mathbf{V}}) - (\hat{\mathbf{L}} \cdot \hat{\mathbf{V}}) \,,$$

where $\hat{\mathbf{V}}$ is the direction from the reflection point to the radiation source. The final form for the Phong reflectance model can be written as the positive part of the $(\hat{\mathbf{R}} \cdot \hat{\mathbf{V}})$ angle:

$$f_{r,\text{Phong}}(\hat{\mathbf{L}}, \hat{\mathbf{V}}, \hat{\mathbf{N}}) = c_p[(2(\hat{\mathbf{N}} \cdot \hat{\mathbf{L}})(\hat{\mathbf{N}} \cdot \hat{\mathbf{V}}) - (\hat{\mathbf{L}} \cdot \hat{\mathbf{V}}))^+]^{c_s} \,.$$

However, several approximations need to be applied in order to calculate reflectivity of the tokamak vessel.

- Light is emitted from the whole volume of the plasma, therefore the number of the light sources is infinite and even after volume discretization, the number of points is intractable by simple ray-tracing. However, the spatial distribution of the emissivity is usually smooth and hence the difference in incident radiance from similar directions is small.
- Multiple reflections were neglected due to insufficient precision in the determination of the models constants, however the contribution can be non-negligible in certain situations.
- Toroidal symmetry is assumed in order to simplify the reflectivity model. Asymmetrical objects such as diagnostics ports were added to the final model.
- The diffusive model is calculated only as a 2D model in the poloidal plane because of the toroidal symmetry.
- The constants c_p, c_l depends on the material surface and it is difficult to measure inside of the tokamak ves-
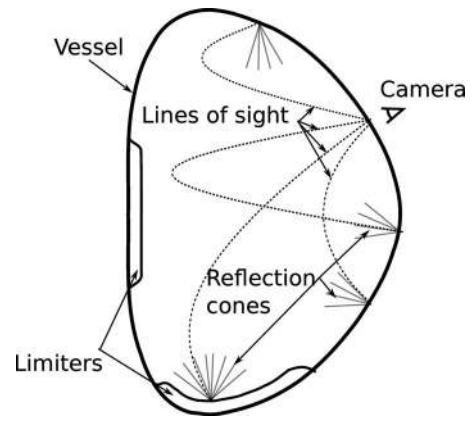

FIG. 2. An example of the camera tomography geometry in the poloidal cross-section of the COMPASS tokamak vacuum vessel with poloidal projections of the lines of sight. The reflectivity of the components depends on the reflecting poloidal angle.

sel, therefore a numerical method for their calculation is proposed.
- The carbon limiter is expected to be a Lambertian object because it has only pure diffuse reflection. Similarly, the diffusive reflection of the metallic vessel was neglected[19] in order to limit the number of searched material constants.

The diffusive model can be calculated under assumption of toroidal symmetry:

$$I_j^L = \sum_i^{N_g} (\hat{\mathbf{L_i}} \cdot \hat{\mathbf{N}}) f_{r,\text{Lambert},j} l_i,$$

where l_i is radiant emissivity from the ith pixel, it corresponds to $g_i / \|\mathbf{V_i}\|$, where $\mathbf{V_i}$ is the direction from the emissivity pixel to the incident point on the vessel wall.

The Phong model is more complicated to calculate. Because the number of light sources is practically intractable, we have used the Helmholtz reciprocity of the BRDF,[19]

$$f_r(\mathbf{L}, \mathbf{V}) = f_r(\mathbf{V}, \mathbf{L}),$$

and viewing cones after the reflection were approximated by a limited number of LoS that were uniformly distributed over the cones of view (Figs. 2 and 3). Therefore, the Phong model
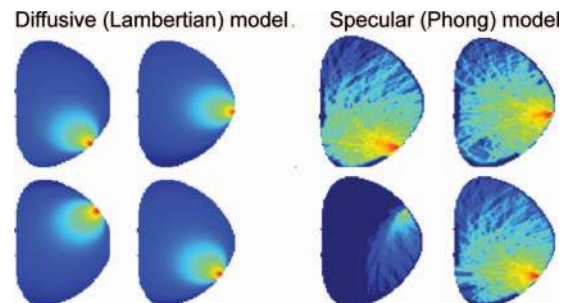

FIG. 3. Examples of origins of the reflected signal using the diffusion model in log-scale. The reflectivity depends on the angle between the ray incident material and reflecting poloidal and toroidal angle.

is calculated as follows:

$$I_j^P = \sum_k^{N_v} \left(f_{r,\text{Phong},k} \sum_i^{N_g} \mathbb{T}_{ij} g_i \right) .$$

N_v denotes the number of chords approximating the reflected cone and $f_j = \sum_i^{N_g} \mathbb{T}_{ij}^{(p)} g_i$ is the radiance produced along the LoS, and $\mathbb{T}_{ij}^{(p)}$ denotes the effect of the ith pixel on the jth reflected ray. The higher order reflections were approximated only by the diffusion model. It turns out that the higher order reflectivity model is usually a minor correction scaled by the factor $c_p \cdot c_l$.

The reflection models are linear maps with respect to the plasma emissivity, therefore the reflected background intensity can be written as

$$f_j^{(r)} = \sum_i^{N_g} \left(c_p \mathbb{M}_{ij}^{(p)} + c_l \mathbb{M}_{ij}^{(l)} \right) g_i = \sum_i^{N_g} \mathbb{M}_{ij} g_i,$$

where $\mathbb{M}_{ij}^{(p)}$ and $\mathbb{M}_{ij}^{(l)}$ are the Phong and the Lambertian reflection matrices and $\mathbf{f}^{(r)}$ is the resulting reflectivity.

Finally, the discussed model includes only toroidally symmetric structures, i.e., vessel and limiter shapes. Asymmetrical reflectivity patterns (e.g., diagnostic ports and some limiters) need to be added. Therefore, an image of the vessel with diffusive light $\mathbf{M}^{(0)}$ was used as a pattern and the resulting reflectivity model $\mathbf{M}$ was locally scaled by this background mask $M^{(0)}$ (see Fig. 4):

$$\mathbb{M}'_{ij} = \mathbb{M}_{ij} M_i^{(0)} .$$

It would be possible to include the reflectivity matrix $\mathbb{M}_{ij}$ directly to the tomographic system Eq. (4), however, $\mathbb{M}_{ij}$ is a dense matrix, while the original geometry matrix $\mathbb{T}_{ij}$ is sparse so that the final system would be difficult to solve. Moreover, the material constants c_p, c_d need to be optimized, so that the following expression was minimized:

$$\min_{c_p, c_d} \left\| \left[\left(c_p \mathbb{M}^{(p)} + c_d \mathbb{M}^{(l)} \right) \mathbf{M}^{(0)} + \mathbb{T} \right] \mathbf{g} - \mathbf{f} \right\| . \quad (7)$$
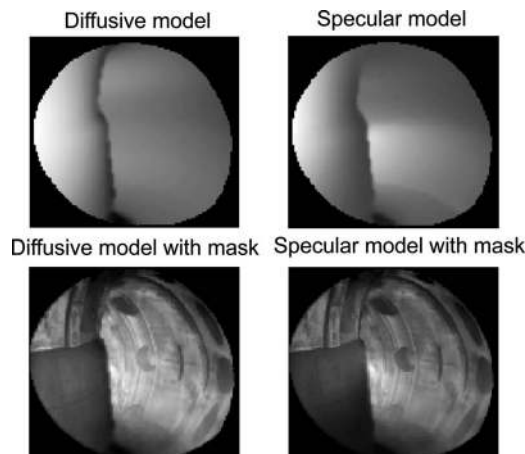

FIG. 4. Calculations of the reflected light using the diffusive and specular reflectivity models.

An asymmetrical L1 norm that prefers positivity was applied in the optimization in order to keep non-negativity and robustness.

IV. APPLICATION ON MEASURED DATA

The major and minor radii of the COMPASS tokamak are 0.56 m and 0.23–0.38 m, respectively. The signal was captured using the EDICAM camera system in resolution 900 × 992 pixels with 1 ms exposure time. The camera is placed at the low field side in a port above the tokamak mid-plane.[14]

The vessel is made mostly from brushed steel with large carbon limiters (see Fig. 2). The Phong reflectivity model was applied on the metallic surfaces, while the Lambertian diffusion model was utilized on the matte carbon limiters (Fig. 4).

We selected a detached circular plasma column located above mid-plane from shot #3487 because the plasma emissivity reconstruction below the mid-plane is proved to be unreliable in the current setup. In the future, the camera will be moved below mid-plane in order to observe the X-point in a divertor configuration of the plasma.

First, the captured image was down-sampled to 124 × 113 pixels due to the fact that the plasma emissivity is flat and smooth. We used only isotropic smoothing in the regularization term $O(\mathbf{g})$. The resolution of the reconstruction was set to 100 × 100 pixels.

The reflectivity model was updated in every iteration using the emissivity from the previous step while optimal reflectivity parameters are searched. Three iterations are usually sufficient for convergence.

V. RESULTS AND DISCUSSION

The reconstructed plasma emissivity (Fig. 5(a)) should have been precisely a circular shape in the reconstructed
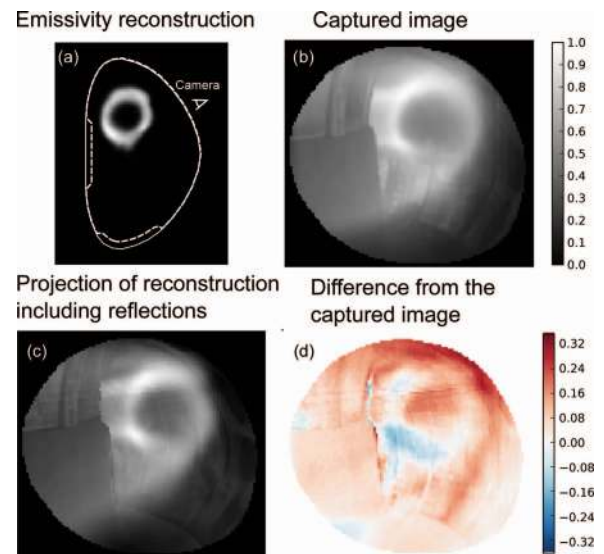

FIG. 5. Plasma emissivity reconstruction from shot #3487 at time 10 ms. The detached plasma column was reconstructed without any assumption about plasma shape from the magnetic equilibrium code. (a) presents our reconstruction, while (b) and (c) show model including background reflections and the measured data. Finally, (d) highlights differences between data and our model.
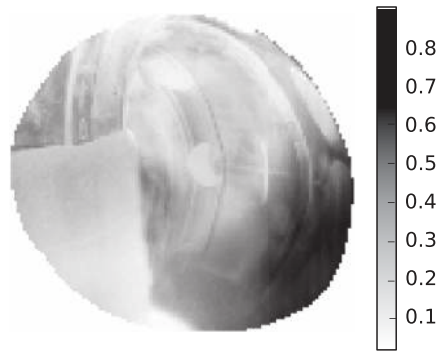
FIG. 6. Ratio between total observed illumination and reflected illumination. The radiation reflected from the chamber wall exceeds the plasma radiation in large areas within the field of view.

FIG. 8. Full lines present the evolution of the Pearson χ^2 distribution depending on the smoothness penalty $\mathbf{g}^*\mathbb{H}\mathbf{g}$ corresponding to the model complexity. The dashed lines correspond to the Hoyer sparsity[20] of the resulting reconstruction. Blue lines with squares display dependence for the original data, while the red lines with circles were obtained after three iterations of the background subtraction algorithm.

shot #3487. However, due to minor imperfection in the geometry setting and reflections subtraction (Fig. 5(d)), the shape is slightly deformed. The difference between our model (Fig. 5(c)) and the original image (Fig. 5(b)) shows that shell radiation was slightly overestimated, while the background radiation was underestimated. This can be explained as radiation of weakly ionized plasma out of the main column.

Particularly, near the center of the plasma column, the difference between retrofit and data is around 20%. Other sources of systematic errors are optical calibration imperfections and the simplicity of our reflective model. It was attempted to use a more complex reflectivity model but it led to less stable and unreliable results.

On the other hand, the reflective model Eq. (7) was able to describe relatively well the reflected light including the local structures, e.g., ports and limiters (Fig. 5(c)). The reflected light forms on the average 35% of the observed luminance and locally it can correspond up to 95% (Fig. 6) of the total luminance.

The background subtraction is a crucial issue. This is shown in terms of the reconstructions with and without the subtraction (Fig. 7). Note that although the difference in the reconstructions is significant (Fig. 7), the Pearson χ^2 criterion Eq. (5) reaches a similar score (see Fig. 8). Note that even the best χ^2 exceeds 10 because of the model imperfections. Furthermore, high-complexity models (high smoothness penalty) lead to worse results because of the non-negativity condition. It can be expected that the ideal reconstruction is relatively sparse with low emissivity values in most of the re-
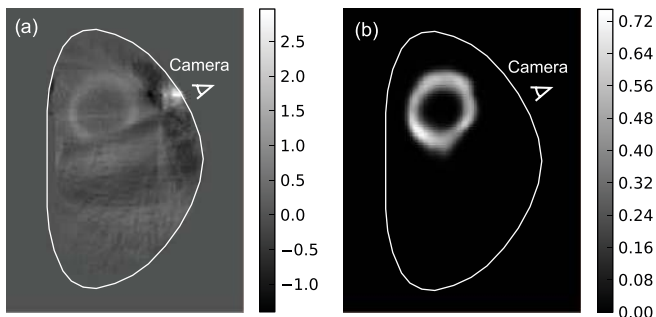
constructed space as it is shown in the Fig. 7. In order to describe the sparsity, we have decided to use the Hoyer sparsity measurement[20, 21] that is defined as a ratio between the $L1$ and $L2$ norm of the data normalized to zero for unitary data and equal to one if all the signal is in one element. The Hoyer sparsity shows significant improvement after the background subtraction and the optimum corresponds to same complexity as the minimal χ^2 value.

VI. CONCLUSION

The proposed background reflection model in combination with some appropriate regularization results in the expected ring shape of the 2D plasma emissivity (Fig. 5(a)). Therefore, the introduced reconstruction scheme including the reflection model is suitable for tangential tomography in tokamaks with metallic vessel and other setup challenges that increase systematic errors.

The regularization Eq. (3) forces emissivity to zero with a non-negative condition. This allows to perform reconstruction despite of systematic errors in input data and iteratively remove background reflections and recover the compact and smooth shape of the plasma emissivity.

In the future, the fast camera in the COMPASS tokamak will be moved to a more suitable position to observe the divertor and a tomographic reconstruction of the plasma divertor legs should be achievable.

FIG. 7. Panel (a) shows reconstruction without background reflection subtraction, while (b) was reconstructed after the background subtraction.
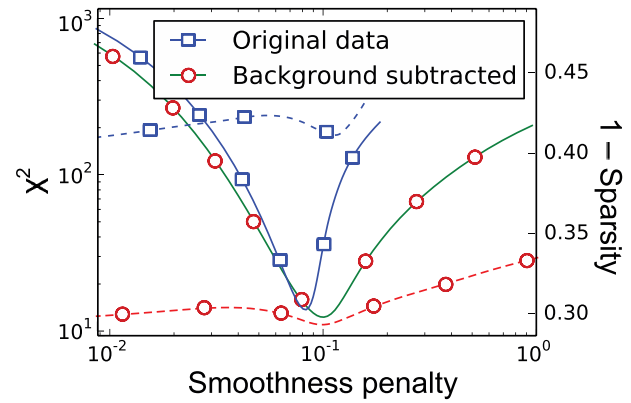
[1]G. Hommen, M. De Baar, P. Nuij, G. McArdle, R. Akers, and M. Steinbuch, "Optical boundary reconstruction of tokamak plasmas for feedback control of plasma position and shape," Rev. Sci. Instrum. **81**(11), 113504 (2010).
[2]R. N. van yen, N. Fedorczak, F. Brochard, G. Bonhomme, K. Schneider, M. Farge, P. Monier-Garbet *et al.*, "Tomographic reconstruction of tokamak

plasma light emission from single image using wavelet-vaguelette decomposition," Nucl. Fusion **52**(1), 013005 (2012).

[3]S. J. Zweben, R. J. Maqueda, D. P. Stotler, A. Keesee, J. Boedo, C. E. Bush, S. M. Kaye, B. LeBlanc, J. L. Lowrance, V. J. Mastrocola *et al.*, "High-speed imaging of edge turbulence in NSTX," Nucl. Fusion **44**(1), 134 (2004).

[4]R. J. Maqueda, G. A. Wurden, S. Zweben, L. Roquemore, H. Kugel, D. Johnson, S. Kaye, S. Sabbagh, and R. Maingi, "Edge turbulence measurements in NSTX by gas puff imaging," Rev. Sci. Instrum. **72**(1), 931–934 (2001).

[5]V. V. Pickalov and G. Fuchs, "Three-dimensional emission tomography of tokamak plasmas with a single tangentially viewing camera," in *Proceedings of the 27th EPS Conference on Controlled Fusion and Plasma Physics, European Conference Abstracts* (2000), Vol. 24, p. 12–16.

[6]D. Iraji, I. Furno, A. Fasoli, and C. Theiler, "Imaging of turbulent structures and tomographic reconstruction of TORPEX plasma emissivity," Phys. Plasmas **17**, 122304 (2010).

[7]L. C. Ingesson, B. Alper, B. J. Peterson, and J.-C. Vallet, "Tomography diagnostics: Bolometry and soft X-ray detection," Fusion Sci. Technol. **53**, 528 (2008).

[8]S. Banerjee, A. K. Chattopadhyay, and P. Vasu, "Tomographic reconstruction of emissivity profile from tangentially viewed images using pixel method," Plasma Fusion Res. **2**, S1120 (2007).

[9]S. Banerjee and P. Vasu, "Diffuse reflection model and noise stabilization for tangential image tomographic reconstruction (TITR) code," Nucl. Fusion **49**(7), 075032 (2009).

[10]T. Odstrcil, M. Odstrcil, O. Grover, V. Svoboda, I. Duran, and J. Mlynar, "Low cost alternative of high speed visible light camera for tokamak experiments," Rev. Sci. Instrum. **83**(10), 10E505 (2012).

[11]P. Lotte, M. Aumeunier, P. Devynck, C. Fenzi, V. Martin, and J. M. Travère, "Wall reflection issues for optical diagnostics in fusion devices," Rev. Sci. Instrum. **81**(10), 10E120 (2010).

[12]K. D. Zastrow, S. R. Keatings, L. Marot, M. G. OMullane, G. de Temmerman, and JET-EFDA Contributors, "Modeling the effect of reflection from metallic walls on spectroscopic measurements," Rev. Sci. Instrum. **79**(10), 10F527 (2008).

[13]G. Thomas, P. Schunke, and B. Huysmans, "Evidence of the influence of reflections on the Zeff profile measurements and their mitigation," in *Proceedings of the 31th EPS Conference on Controlled Fusion and Plasma Physics, European Conference Abstracts* (2004), Vol. 28.

[14]A. Szappanos, M. Berta, M. Hron, R. Pánek, J. Stöckel, S. Tulipán, G. Veres, V. Weinzettl, and S. Zoletnik, "EDICAM fast video diagnostic installation on the COMPASS tokamak," Fusion Eng. Des. **85**(3), 370–373 (2010).

[15]J. Mlynar, V. Weinzettl, G. Bonheure, and A. Murari, "Inversion techniques in the soft-X-ray tomography of fusion plasmas: Toward real-time applications," Fusion Sci. Technol. **58**(3), 733–741 (2010).

[16]M. Anton, H. Weisen, M. J. Dutch, W. Linden, F. Buhlmann, R. Chavan, B. Marletaz, P. Marmillod, and P. Paris, "X-ray tomography on the TCV tokamak," Plasma Phys. Controll. Fusion **38**, 1849 (1996).

[17]J. Mlynar, S. Coda, A. Degeling, B. P. Duval, F. Hofmann, T. Goodman, J. B. Lister, X. Llobet, and H. Weisen, "Investigation of the consistency of magnetic and soft x-ray plasma position measurements on TCV by means of a rapid tomographic inversion algorithm," Plasma Phys. Controll. Fusion **45**, 169 (2003).

[18]M. Odstrcil, J. Mlynar, T. Odstrcil, B. Alper, and A. Murari, "Modern numerical methods for plasma tomography optimisation," Nucl. Instrum. Meth. Phys. Res. Sec. A **686**, 156–161 (2012).

[19]L. Neumann, A. Neumannn, and L. Szirmay-Kalos, "Compact metallic reflectance models," in *Computer Graphics Forum* (Wiley Online Library, 1999), Vol. 18, pp. 161–172.

[20]N. Hurley and S. Rickard, "Comparing measures of sparsity," IEEE: Trans. Inform. Theory **55**(10), 4723–4741 (2009).

[21]P. O. Hoyer, "Non-negative sparse coding," in *Neural Networks for Signal Processing* (IEEE, 2002).